Project: **SEAWave**

Microscopic dosimetry of skin models and its maximisation

Work Package: WP5

Deliverable: D5.3

Deliverable No.: D17

Abstract

The proliferation of millimeter-wave technologies, particularly in 5G and beyond, has increased the need to quantify electromagnetic energy deposition in human skin, the primary site of exposure. This deliverable presents a framework for constructing realistic 3D skin models based on high-resolution Optical Coherence Tomography OCT and Ultrasound imaging, capturing site-specific anatomical variability, microstructures such as sweat gland ducts, and pathological conditions including Basal Cell Carcinoma (BCC). Finite-Difference Time-Domain simulations were performed in the 20–40 GHz range, with emphasis on 27.5 GHz, to evaluate electric field and specific absorption rate (SAR) distributions. Results show that realistic skin geometries produce highly non-uniform exposure conditions compared to simplified planar models. For example, in the viable epidermis the ratio of maximum-to-minimum electric field values increases from 1.5 in planar models to 7.2 in realistic models, highlighting the role of undulating skin interfaces. Frequency dependence was also observed, with this ratio decreasing slightly to 6.7 at 40 GHz. Sweat gland ducts exhibited localized SAR values nearly twice those of the surrounding viable epidermis (1.86 mW/kg vs. 0.99 mW/kg), while pathological conditions such as BCC caused moderate shifts in reflected fields and reduced superficial SAR. Overall, the methodology presented in this deliverable advances microdosimetric precision, supports individualized exposure assessment within the SEAWave-clin study, and provides quantitative guidance for the development of simplified equivalent phantoms for compliance testing.

Project Details

Project name	SEAWave
Grant number	101057622
Start Date	01 Jun 2022
Duration	42 months
Scientific coordinator	Prof. Th. Samaras, Aristotle University of Thessaloniki (AUTH)

Deliverable Details

Deliverable related number	D5.3
Deliverable No.	D17

Deliverable name	Microscopic dosimetry of skin models and its maximisation
Work Package number	WP5
Work Package name	Macro and Microdosimetry in the Human and Murine Skin
Editors	Iakovidis S, Samaras T
Distribution	Public
Version	1.0
Draft/final	Final
Keywords	Dosimetry, microdosimetry, skin exposure, mmWave, realistic skin models

Contents

1 Introduction

The rapid development of millimeter-wave (MMW) technologies, particularly in 5G and beyond, has raised concerns about their interaction with human tissue, especially the skin. The lower wavelength of MMW, results in significantly lower penetration depth in human tissues [1]. Thus, skin as the outermost tissue of the human body, is dominantly exposed and consequently studied [2]. The current work within WP5, presents a comprehensive dosimetric investigation into MMW energy deposition in human skin using realistic 3D models. These models, constructed from Optical Coherence Tomography (OCT) and Ultrasound (US) imaging data, capture anatomical detail across different body sites and skin microstructures. By applying Finite-Difference in Time-Domain (FDTD) simulations, focusing on 27.5 GHz — the frequency used in the SEAWave-clin study — our research evaluates how variations in skin geometry and pathology influence energy absorption. The findings support individualized dosimetry and inform simplified phantom models for compliance testing.

2 Objective

The present deliverable aims to advance the understanding of energy deposition in human skin at millimeter waves (MMWs). To this end, realistic 3D skin models have been developed to enable detailed dosimetric characterization (i.e., microdosimetry) of human skin. The influence of skin layer undulation and microstructures on the maximisation of energy absorption is investigated. The methodology established here also supports individualized dosimetric assessments, which are applied to participants in the SEAWave-clin study (WP7). Finally, the microdosimetry results contribute to the determination of simplified equivalent phantom requirements for compliance testing (WP4).

3 Materials and Methods

A framework for building realistic 3D human skin models, based on Optical Coherence Tomography (OCT) and Ultrasound (US) imaging data, is initially developed. This framework is then used to generate skin models representing different body sites. The resulting models are employed for dosimetric analysis using the FDTD method. Simulations are conducted at various frequencies within the MMW band, with particular emphasis on 27.5 GHz, the frequency used in the SEAWave-clin study. Additional models incorporating skin microstructures (i.e., sweat gland ducts) and pathological conditions (i.e., Basal Cell Carcinoma, BCC) are also developed, and their impact on dosimetry maximisation is evaluated.

3.1 Model building framework

Optical Coherence Tomography is a medical imaging technique based on the principle of Michelson interferometry, commonly used for non-invasive investigation of tissues in ophthalmology and dermatology [28]. The resolution of an OCT scan image ranges from 1μm for ultra-high-resolution systems (e.g., LC-OCT [29]) to around 20μm and is superior to that achieved by other tomographic methods such as conventional ultrasound [30]. On the other hand, it offers a moderate penetration depth of approximately 1.5mm [28]. OCT enables the visualization of different skin strata (e.g., stratum corneum (SC), epidermis, dermis) and some cutaneous appendages (e.g., hair follicles, eccrine sweat ducts, sebaceous glands) [30]. It also provides useful visual information pertaining to inflammatory skin diseases and tumours [28].

Compared to OCT, US imaging offers a substantially higher penetration depth at the expense of reduced resolution. For instance, a 15MHz ultrasound device has a penetration depth of approximately 2.5cm and a resolution of 0.1mm [31]. Consequently, US can provide imaging of deep skin regions (e.g., deep dermis (DE)) and subcutaneous tissues (e.g., fat (FT), muscle (MS), bone (BN)) but with substantially lower detail compared to OCT.

The proposed framework for realistic 3D skin model building consists of 3 major steps: (a) OCT and US image acquisition, (b) image processing (measurement and segmentation), and (c) processed data synthesis (Figure 1).

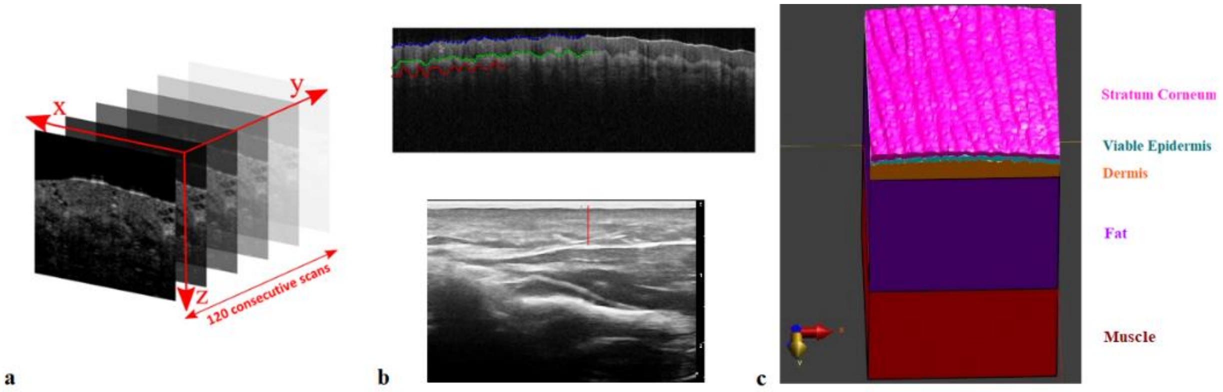

Figure 1. Steps for 3D skin model building: (a) OCT and US image acquisition, (b) segmentation of OCT scan images (top) and measurement (bottom) of the distance from air to dermis-fat interface (green) and air to fat-muscle interface (red), and (c) data synthesis and 3D model generation.

The image acquisition process includes OCT and US scanning of the target skin region. In our project, the OCT scans were performed using a multi-beam, swept-source system from Vivosight (Vivosight, Michelson DiagnosticTM Inc., Kent, United Kingdom). The scanning area was 6mm × 6mm and 120 consecutive images of skin vertical cross sections (Figure 1b, top) were acquired, offering a resolution of approximately 5μm × 50μm × 5μm up to a depth of 1mm. The US images

(Figure 1b, bottom) were acquired using an Esaote MyLab X6 system (Esaote S.p.A., Genoa, Italy) with a transducer (AL2442), offering a resolution of 0.1mm up to a depth of 30mm.

The segmentation process involves the OCT images only. Based on the identification of skin layers presented in [30] for different body sites, three interfaces are identified and marked on each OCT image (Figure 1b, top): (a) air-SC, (b) SC-VE, and (c) VE-DE (dermoepidermal junction, DEJ). The data for each of the 3 interfaces mentioned above, are then combined for the 120 consecutive images (Figure 1a) to form three different surfaces, using code developed in MATLAB (The MathWorks Inc., Natick, MA, USA). It should be noted here that the US imaging, due to its higher penetration depth compared to OCT, is used only for the measurement of the thicknesses of DE and FT layer. However, the significantly lower resolution of US does not allow for accurate 3D model building. Consequently, the DE-FT and FT-MS interfaces are considered planar (Figure 1).

The three different skin interfaces produced in the segmentation process above are then imported, in an STL (stereolithography) file format, into Sim4Life (ZMT, Switzerland) software. Using the CAD tools available and the US imaging measurements, the final 3D model is constructed (Figure 1c).

Except for the geometric model, an electromagnetic simulation requires the definition of the dielectric properties (i.e., permittivity, electrical conductivity) of its constituting materials (skin and subcutaneous layers). Therefore, the permittivity and electrical conductivity of SC, VE, DE, FT, BN and MS layers need to be defined.

SC is the outermost skin layer consisting of keratinized cells with a low water content [1], [10]. The dielectric parameters used in [1], [9], [10], are applied. The remaining part of the epidermis, called viable epidermis (VE), has no blood supply, yet significantly higher water content [1]. Dermis (DE), the outermost perfused skin layer, has a water content close to that of VE [10] which has led to the use of identical dielectric properties for these two distinct layers in [1], [9], [10]. However, in vivo confocal Raman spectroscopy measurements of water content in human forearm skin [32], show, except for a dramatic increase from SC to VE, a small increase as depth increases thereafter. This could be reasonably attributed to the DE layer, which is in line with the measurements in [33] that are also applied here. Dielectric parameters evaluated at 27.5 GHz are shown in Table 1.

Table 1. Relative permittivity, conductivity and mass density values for each skin layer and subcutaneous layers at 27.5GHz

Skin / subcutaneous layer	Relative permittivity	Conductivity (S/m)	Mass density (kg/m^3)
SC, stratum corneum	3.58	1.13	1500
VE, viable epidermis	16.66	19.28	1109
DE, dermis	19.63	24.40	1109
FT, fat	3.54	2.19	911
MS, muscle	23.53	37.42	1090
BN, bone (cortical) [36]	5.21	4.89	1908

3.2 Skin models

Following the procedure described above, three different skin models of a healthy middle-aged Caucasian male volunteer were created: (a) hypothenar region (Figure 2a), (b) volar forearm (Figure 2b), and (c) fingertip (Figure 2c).

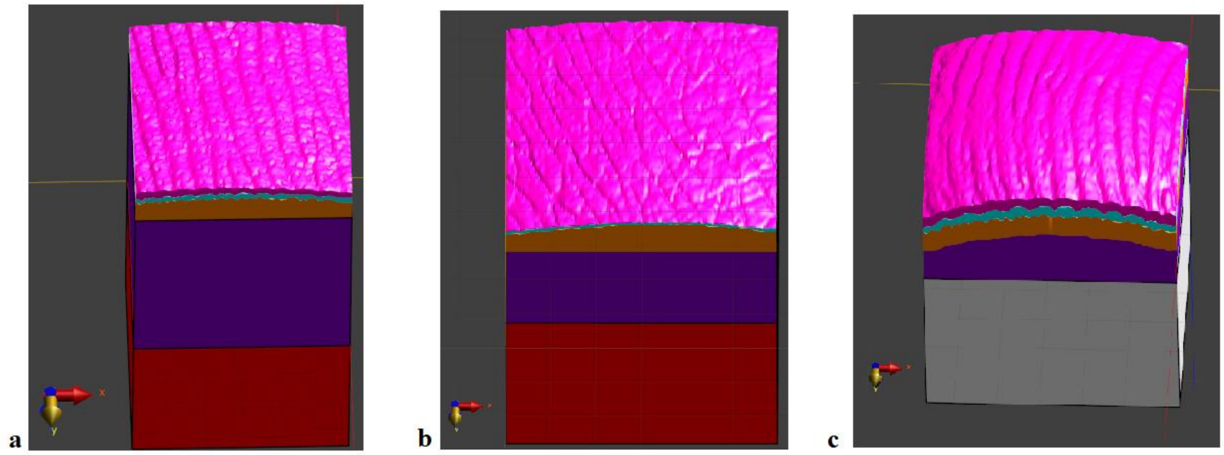

Figure 2. 3D skin models for 3 different body sites: (a) hypothenar region, (b) volar forearm, (c) fingertip. Skin and subcutaneous layers are marked with different colours: SC (pink), VE (cyan), DE (orange), FT (purple), MS (dark red) and BN (white).

Cases (a) and (c) correspond to "thick skin" and case (b) to "thin skin" [30], as can be observed in terms of SC and VE thicknesses in Figure 2. Skin ridges (cases (a) and (c)) and sweat pores (case (a)) are also identifiable. This fact enables the realistic positioning of sweat gland ducts (acrosyringium) beneath each sweat pore (Figure 3a). This skin appendage is of particular interest from a dosimetry point of view, due to its helical structure and dielectric properties [5], [6], [7],

[8], [12], [35]. Different roughness of skin interfaces at different body sites is also captured using the proposed method (e.g., Figure 2c, higher undulation of superficial skin layers at the fingertip).

Table 2. Thicknesses (μm) of skin and subcutaneous layers for the 3 different 3D models

Skin / subcutaneous layer	**Hypothenar region** (μm)	**Volar forearm** (μm)	**Fingertip** (μm)
SC, stratum corneum [37], [38]	267.9	21.5	317.3
VE, viable epidermis [39], [40]	156.6	88.4	264.6
DE, dermis [40], [41]	775.5	830.2	618.1
FT, fat	5100.0	2360.0	1500.0
MS, muscle	4000.0	4000.0	-
BN, bone	-	-	4000.0

The roughness of the air-skin interface and the dermoepidermal junction was calculated as a measure of the undulating nature of the superficial skin layers and is presented in Table 3. The surface characterization is based on the vertical deviations of the roughness profile from the mean line. R_a is the arithmetic mean deviation, i.e., the arithmetic average of profile height deviations from the mean line. R_q is the quadratic mean, i.e., the root-mean-square average of profile height deviations from the mean line [42]. It is clear that the site of the volar forearm presents the smallest roughness at the surface of the skin (air-skin interface), but also further inside at the dermoepidermal junction (DEJ).

Table 3. Roughness of skin interfaces for the 3 different 3D models

Interface	**Roughness measure**	**Fingertip**	**Hypothenar region**	**Volar forearm**
Air-skin interface	R_a (μm)	37.6	27.7	11.2
	R_q (μm)	46.7	33.7	14.3
Dermoepidermal junction	R_a (μm)	14.6	14.6	10.8
	R_q (μm)	17.3	17.0	13.4

Two additional skin models were developed: (a) a model of the hypothenar skin region including sweat gland ducts (acrosyringium) (Figure 3a), and (b) a model of a "thin" skin region containing a nodular Basal Cell Carcinoma (BCC) (Figure 3b). Although realistic modeling of a sweat gland duct is not feasible using OCT data due to its complex helical structure, realistic placement of a manually designed duct beneath a sweat pore is achievable, thanks to the identifiable sweat pores in our models. The dimensional and dielectric properties of the sweat gland duct were obtained from the literature [6], [7], [35], and are as follows: (a) helical duct length=Epidermis (SC+VE) thickness, (b) helix diameter = 100μm, (c) cross-sectional diameter = 25μm, (d) Distance between turns = 70μm and (e) sweat dielectric properties at 27.5 GHz ($\varepsilon_r = 24.64$, $\sigma = 52.43$ S/m). For the BCC skin model, the dimensional data of the region containing BCC tumor islands were derived from segmentation of OCT scan images, while the dielectric properties were taken from [43].

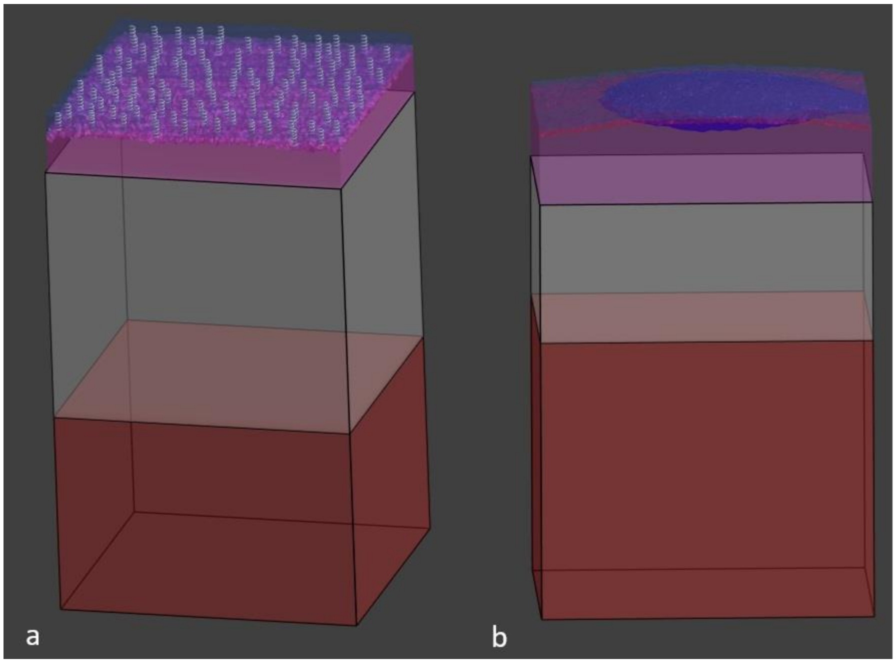

Figure 3. 3D skin models for: (a) hypothenar region including sweat gland ducts (left) and (b) pathological skin, i.e., nodular BCC, (right).

3.3 Electromagnetic simulation

The electromagnetic (EM) simulation was performed using the FDTD method, implemented in the Sim4Life software platform. A linearly polarized plane wave source of 1 V/m in amplitude, propagating along z-axis, with the electric field (E-field) vector parallel to the x-axis, was used (TE-polarization). At 27.5 GHz, for the fingertip model (Figure 2c), the lower wavelength inside the tissues is that of dermis:

$$\lambda_{DE} = \frac{\lambda_0}{\sqrt{\varepsilon_{DE}}} = 2.46\text{mm} \tag{1}$$

where λ_0 the wavelength in free space, λ_{DE} the wavelength in dermis layer, and ε_{DE} the relative permittivity of dermis layer. A common practice is to select the grid size of the computational domain so that the $\lambda/10$ rule-of-thumb is satisfied to reduce numerical dispersion of the FDTD method [44], [45]. However, in order to capture the model's structural details, a grid size of 0.02mm was selected as will be explained later in more detail. Perfectly Matched Layers (PMLs) were applied at the top and bottom of the model (parallel to xy plane) and Periodic Boundary Conditions (PBCs) on the sides (parallel to xz and parallel to yz planes). The application of PBCs assumes that a single unit cell of the computational domain can be simulated instead of a large periodic structure [46]. However, in our case the single unit cell is neither perfectly symmetric nor can it reproduce the large-scale geometry of a fingertip when repeated in space. To avoid the aforementioned problem, the following approach is followed: The large-scale curvature of the model is initially removed by detrending, then corrected for distortion and finally mirrored sequentially at planes parallel to xz and yz planes. Thus, a flat (in terms of large-scale curvature), undistorted and symmetric unit cell of the computational domain, appropriate for PBCs application is created. This procedure and its impact on the E-field distribution in the VE layer is shown in Figures 4 and 5, respectively. It should be mentioned that this model is considered appropriate for assessing the variations in dosimetry resulting from the undulating boundaries of the skin layers only, i.e., the small-scale curvature of skin layers (thus, only fit for assessing micro-dosimetry), under plane wave incidence, and not for assessing the variations in dosimetry due to the large-scale skin curvature that changes at different body locations.

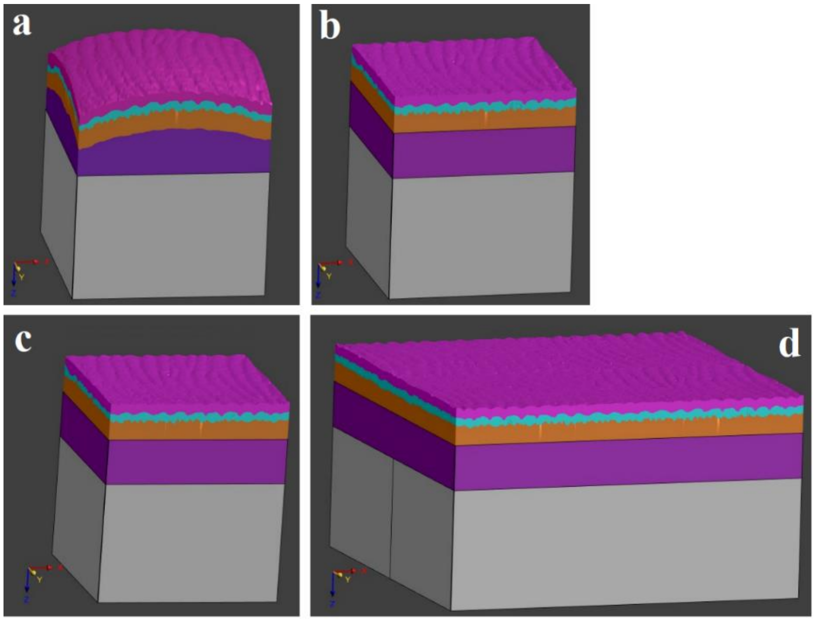

Figure 4. Fingertip skin model alteration procedure to apply PBCs: (a) original model, (b) flattened model (produced by detrending), (c) flattened and undistorted model, and (d) symmetric model (produced by mirroring model c)

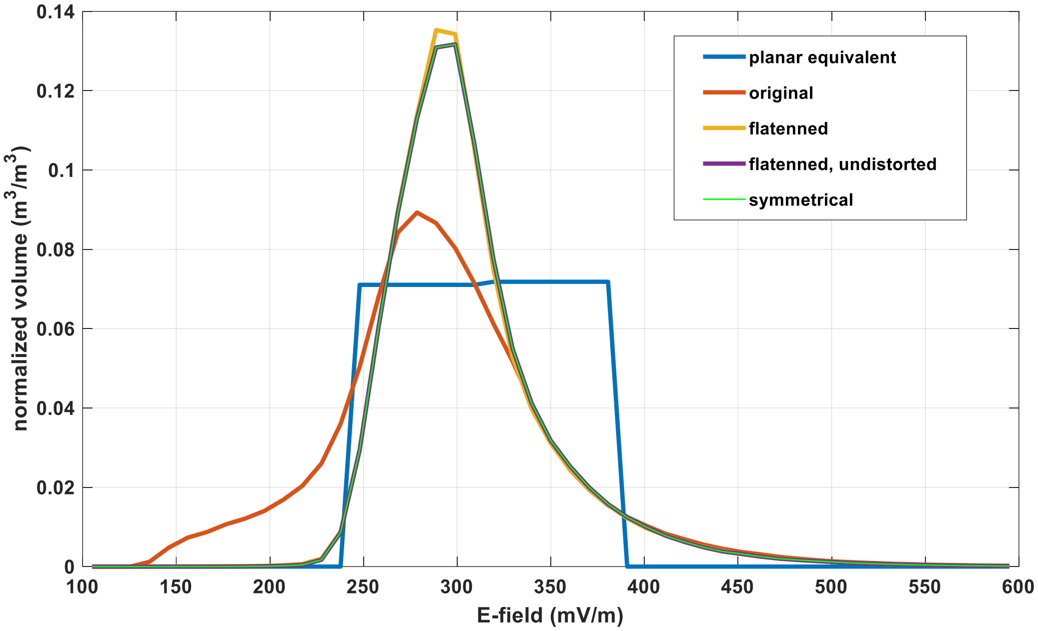

Figure 5. E-field distribution inside the VE skin layer per area volume (normalized), for various skin models of the fingertip presented in Figure 3 plus a planar equivalent model.

Taking a closer look at the E-field distribution per volume area for the VE skin layer (Figure 5) we can make the following comments:

a) The E-field distributions of all models (Figure 4) depart significantly from the one in the planar equivalent model (i.e., the model with planar interfaces of skin layers and equal volume (for each layer) with the original one) and include both lower and higher E-field values.

b) The broadening of the E-field distribution in the original model is significantly reduced in the flattened models. This fact highlights the necessity of flattening the original model in order to simulate a small skin sample by applying PBCs and avoiding large errors induced by repeating a non-symmetric cell.

c) The removal of the distortion produced in the flattening procedure further enhances dosimetry.

d) The consideration of a symmetric model (Figure 3d) has only a marginal impact on dosimetry. As a result, the flattened-undistorted model can be considered sufficient, also offering the advantage of reducing computational resources by a factor of 4 compared to the symmetric one.

Additionally, the impact of the grid size on dosimetry metrics (i.e., E-field) was evaluated. A uniform grid was applied, and the grid step was progressively decreased (λ_{DE} /5, λ_{DE} /10, λ_{DE}/40, and λ_{DE}/400, where λ_{DE} is the wavelength inside DE layer, that is the minimum wavelength inside tissue for the fingertip model) and the variations of the E-field distribution (normalized per volume area), for plane wave incidence of 1 V/m in amplitude, were studied (Figure 6).

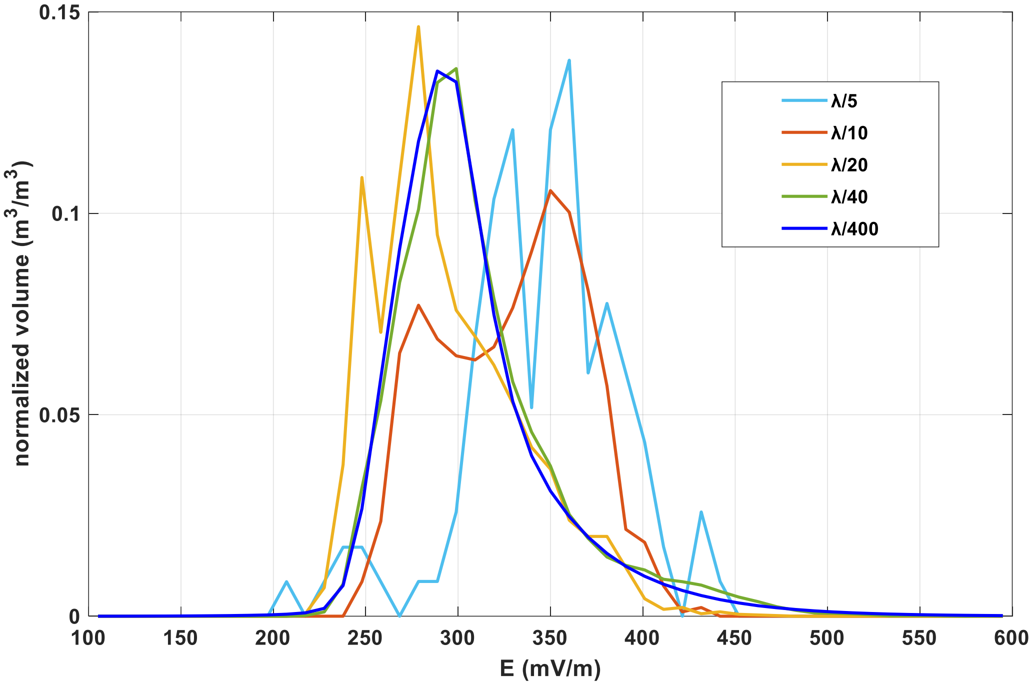

Figure 6. E-field distribution PDF normalized per volume for different grid sizes, inside the VE layer for the flattened-undistorted model of the fingertip. Grid size is expressed as a fraction of minimum wavelength inside tissue (λ).

Figure 6 shows that the distribution of E-field values inside VE layer converges for grid step lower than $\lambda_{DE}/40$ (i.e., 62μm). This value is lower than $\lambda_{DE}/10$ which is often used for homogenous media [45], [46]. This very small grid step is necessary to efficiently capture the model resolution (5μm × 50μm × 5μm) and the thicknesses of the skin layers (Table 2). Yet, the resulting, computationally intensive grid can be mitigated using other techniques (e.g., non-uniform grid). The value of 20μm was selected for the grid step, as a compromise between computational error and required simulation time.

4 Results and Discussion

As can be inferred from Figure 5, the distribution of the E-field values in the fingertip 3D model departs from the one resulting from the planar model used widely in the literature. This fact can also be observed in Figure 7 and Table 4 regarding both E-field and SAR values.

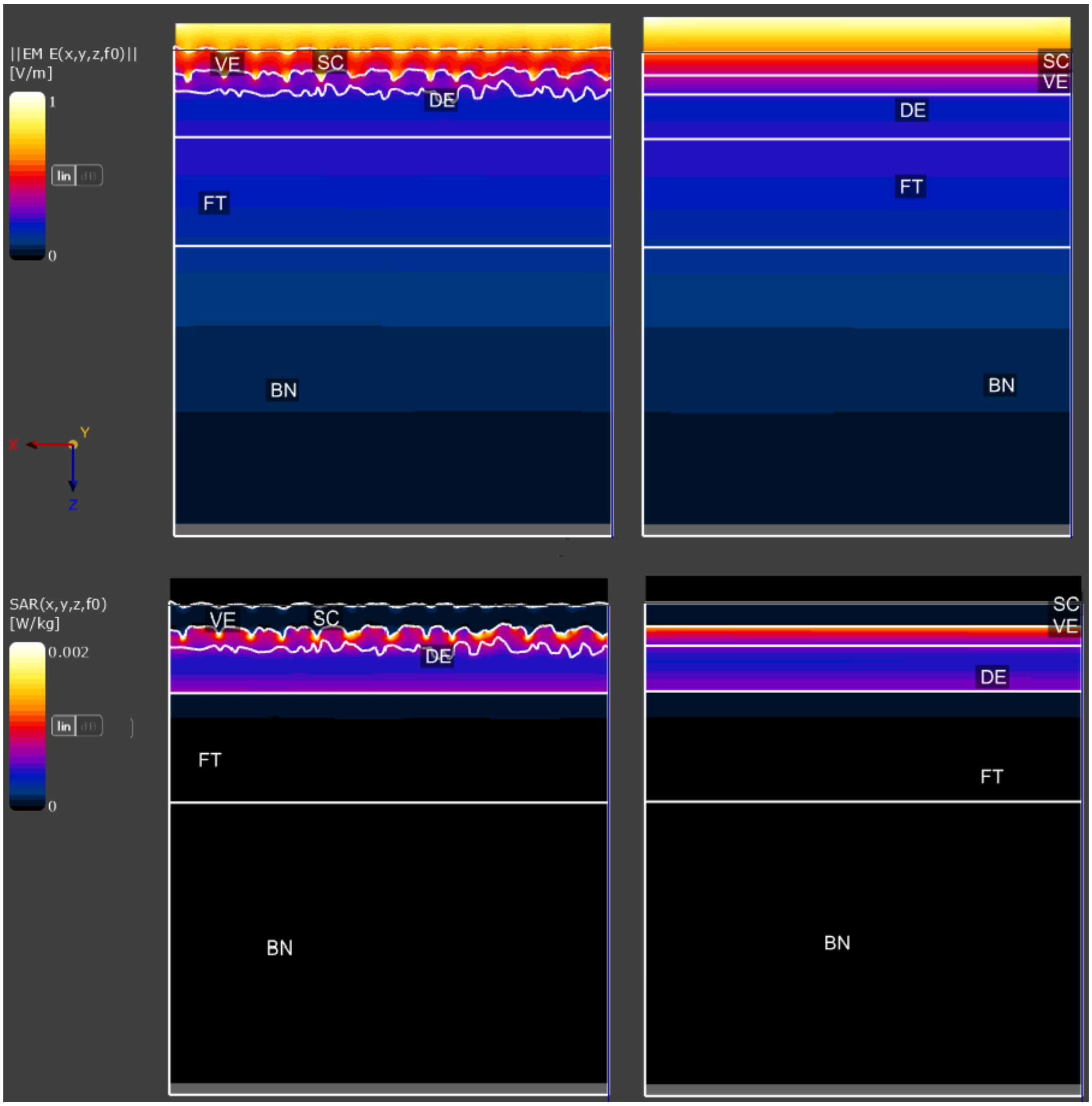

Figure 7. Colormaps of E-field (up) and SAR (down) values in a plane parallel to the xz-plane for the fingertip models: realistic (left) and planar (right). Values correspond to an incident plane wave of 1V/m in amplitude and 27.5 GHz in frequency, propagating along z axis. The E-field is linearly polarized parallel to x axis.

Table 4. The statistical comparison of E and SAR values between the two different models of the fingertip

	Planar Equivalent model				3D Realistic model			
E-field Statistics (V/m) / Skin Layer	min	max	mean	std	min	max	mean	std
Stratum Corneum	0.392	0.588	0.486	0.060	0.193	1.200	0.514	0.070
Viable Epidermis	0.250	0.382	0.314	0.041	0.107	0.769	0.308	0.045
Dermis	0.202	0.243	0.221	0.014	0.193	0.337	0.222	0.015
Fat	0.147	0.240	0.201	0.029	0.147	0.241	0.200	0.029
Bone	0.034	0.146	0.076	0.032	0.034	0.147	0.075	0.032
SAR Statistics (mW/kg) / Skin Layer	min	max	mean	std	min	max	mean	std
Stratum Corneum	0.058	0.130	0.091	0.022	0.014	0.543	0.101	0.027
Viable Epidermis	0.544	1.271	0.872	0.227	0.100	5.146	0.843	0.273
Dermis	0.437	0.634	0.526	0.067	0.412	1.250	0.546	0.074
Fat	0.026	0.070	0.049	0.014	0.026	0.070	0.049	0.014
Bone	0.001	0.027	0.009	0.007	0.001	0.028	0.009	0.007

E-field and SAR values in Table 4 and Figure 7 show differences in dosimetry when considering a 3D skin model, compared to the planar one. These differences are larger for the SC and VE layers, lower in DE and marginal for subcutaneous layers (FT, MS and BN). The differences refer to the minimum, maximum and standard deviation of the distribution, while mean values are largely maintained. For example, in the case of the finger and inside the VE layer, the ratio $\frac{E_{max}}{E_{min}}$ takes a value of 7.2 in the realistic 3D model, compared to 1.5 in the planar equivalent model. This difference shows that the microgeometry of the skin layers interfaces, which is present in the 3D model, describes the actual exposure conditions in the skin, which can be highly non-uniform. The biological significance of this finding remains to be investigated, but the maximum values of the electric field appear in the areas where critical cell types are located, i.e., at the basal layer of the VE (basal cells, melanocytes, Merkel cells) or slightly above it in the stratum spinosum (squamous cells). Moreover, in the VE region several free nerve endings and keratinocytes lie, which play an important role to nociception and neuroinflammation [49].

Figure 8 shows the absorbed energy pattern for three different body sites at 27.5 GHz. Higher thicknesses of both SC and VE layers in “thick skin” areas (i.e., fingertip, hypothenar region) compared to “thin skin” areas (i.e., forearm) result in higher E-field values in the upper part of the DE layer.

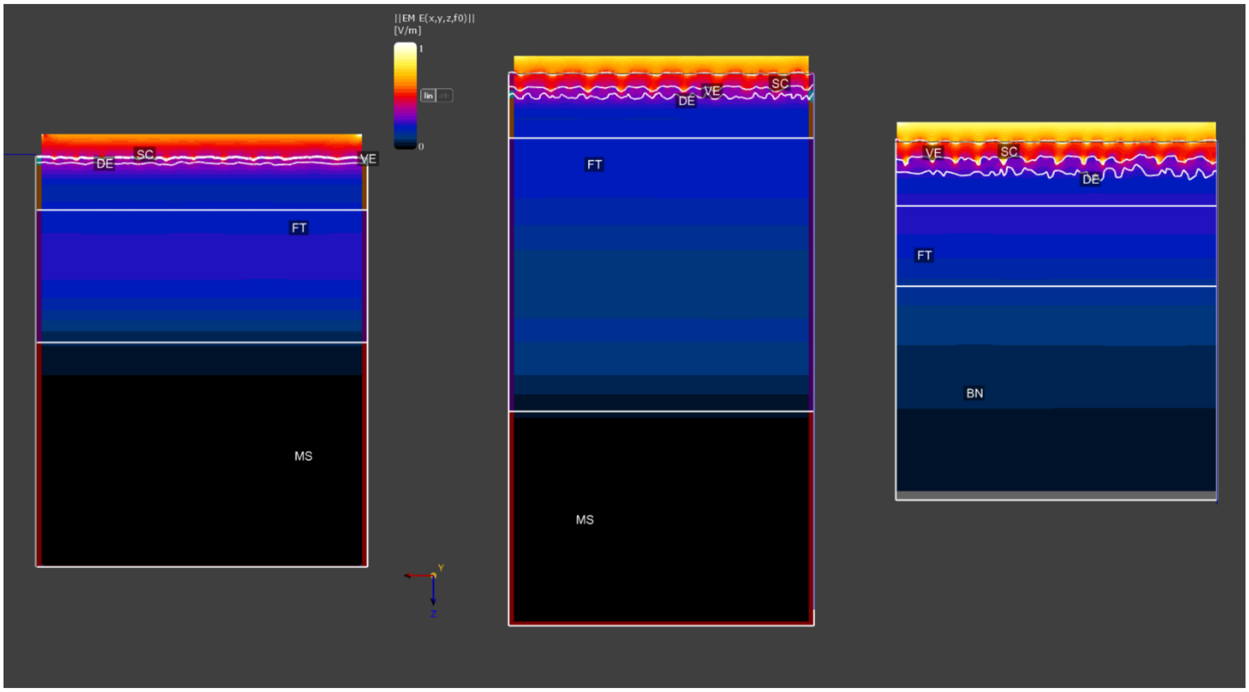

Figure 8. Colormaps of E-field values inside realistic 3D skin models at a plane parallel to the xz-plane for different body sites: (a) volar forearm (left), (b) hypothenar region (center), and (c) fingertip (right). Values correspond to an incident plane wave of 1V/m in amplitude and 27.5 GHz in frequency, propagating along z axis. The E-field is linearly polarized parallel to x axis.

Figure 8 shows that large differences in skin layers thicknesses and boundaries are present between different body sites. A remarkable difference in SC thickness is also obvious between thick skin (fingertip, hypothenar region) and thin skin (volar forearm). The impact of the aforementioned differences and skin layers interfaces’ geometry on dosimetry can be observed in the colourmaps.

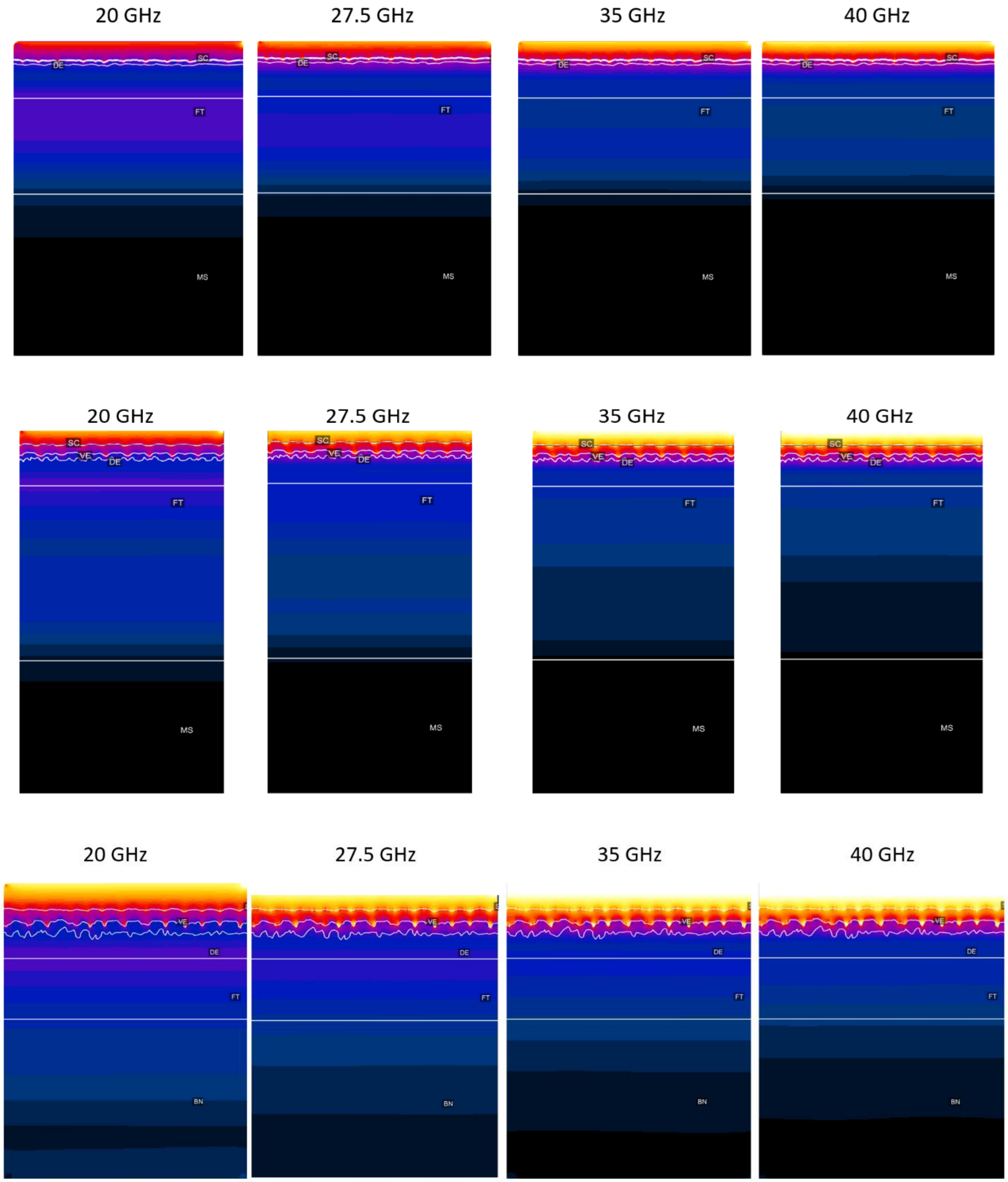

Figure 9. Colormaps of E-field values inside realistic 3D skin models at a plane parallel to the xz-plane for different body sites: (a) volar forearm (top), (b) hypothenar region (center), and (c) fingertip (bottom). Values correspond to an incident plane wave of 1V/m in amplitude and 4 different values of frequency (i.e., 20 GHz, 27.5 GHz, 35GHz and 40 GHz), propagating along z axis. The E-field is linearly polarized parallel to x axis.

Figure 9 shows the absorbed energy pattern for the 3 models above but for different frequencies (i.e., 20 GHz, 27.5 GHz, 35GHz and 40 GHz). The maximum E-field value in the model increases with frequency, however the ratio $\frac{E_{max}}{E_{min}}$ does not change a lot, because the minimum E-field also becomes larger. The ratio decreases from 7.2 to 7.1 and subsequently to 6.7 as the frequency increases from 27.5 GHz to 35 GHz and then to 40 GHz.

The inclusion of sweat gland ducts (acrosyringia) has only a moderate impact on the E-field distribution, which is affected only at locations in very close proximity to the ducts (Figure 10).

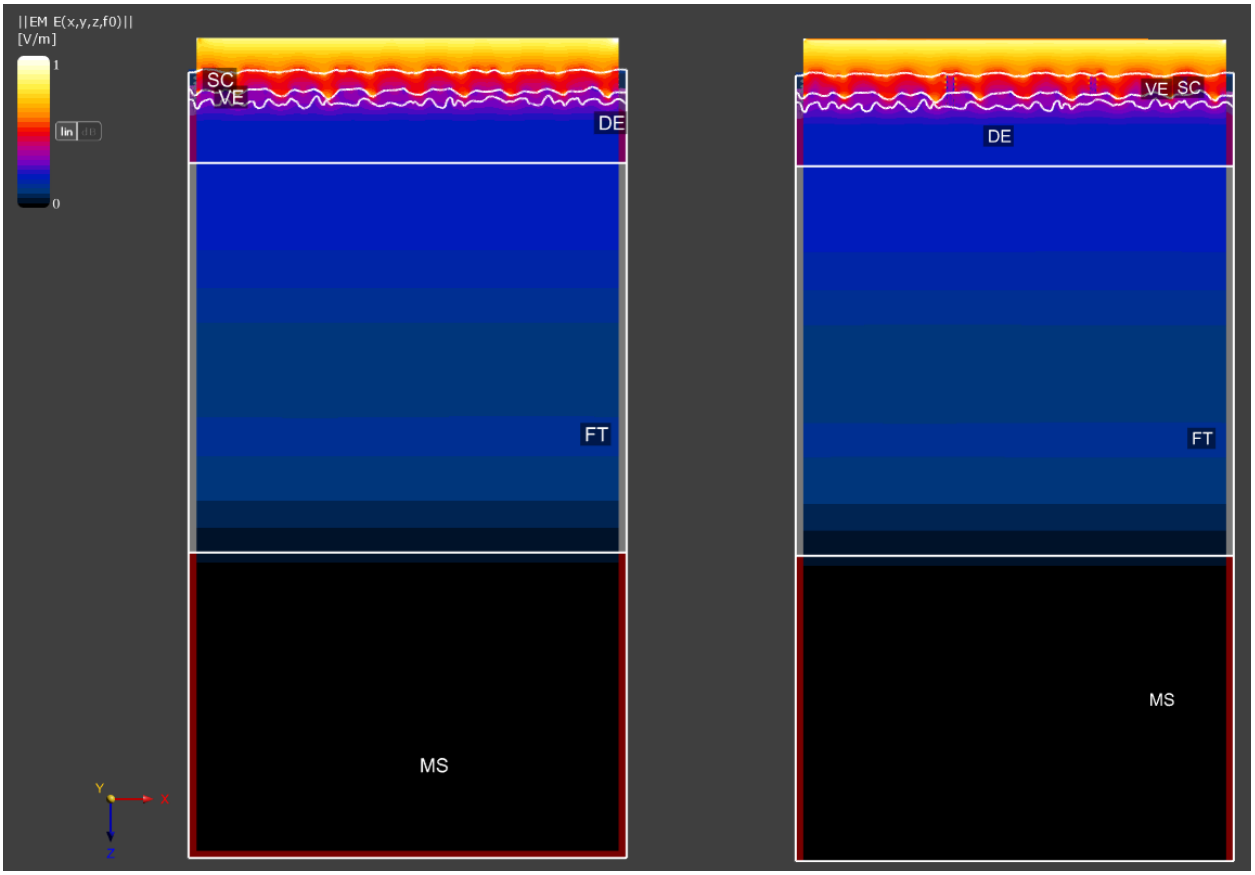

Figure 10. Colormaps of E-field values inside realistic 3D skin models at a plane parallel to the xz-plane for hypothenar region (center), and (c) fingertip (bottom). Values correspond to an incident plane wave of 1V/m in amplitude and 27.5 GHz in frequency, propagating along z axis. The E-field is linearly polarized parallel to x axis.

However, the SAR distribution inside the glands, especially the SAR values evaluated for sweat, differ substantially compared to the SAR values of the surrounding tissue, either SC or VE. This can be seen in the colourmaps of Figure 11 and in Table 5. Note that the mass-averaged SAR value reported in Table 5 is the median value among the mass-averaged SAR values for all 115 sweat gland ducts included in the skin model, either for the inner or the outer part of the helical duct.

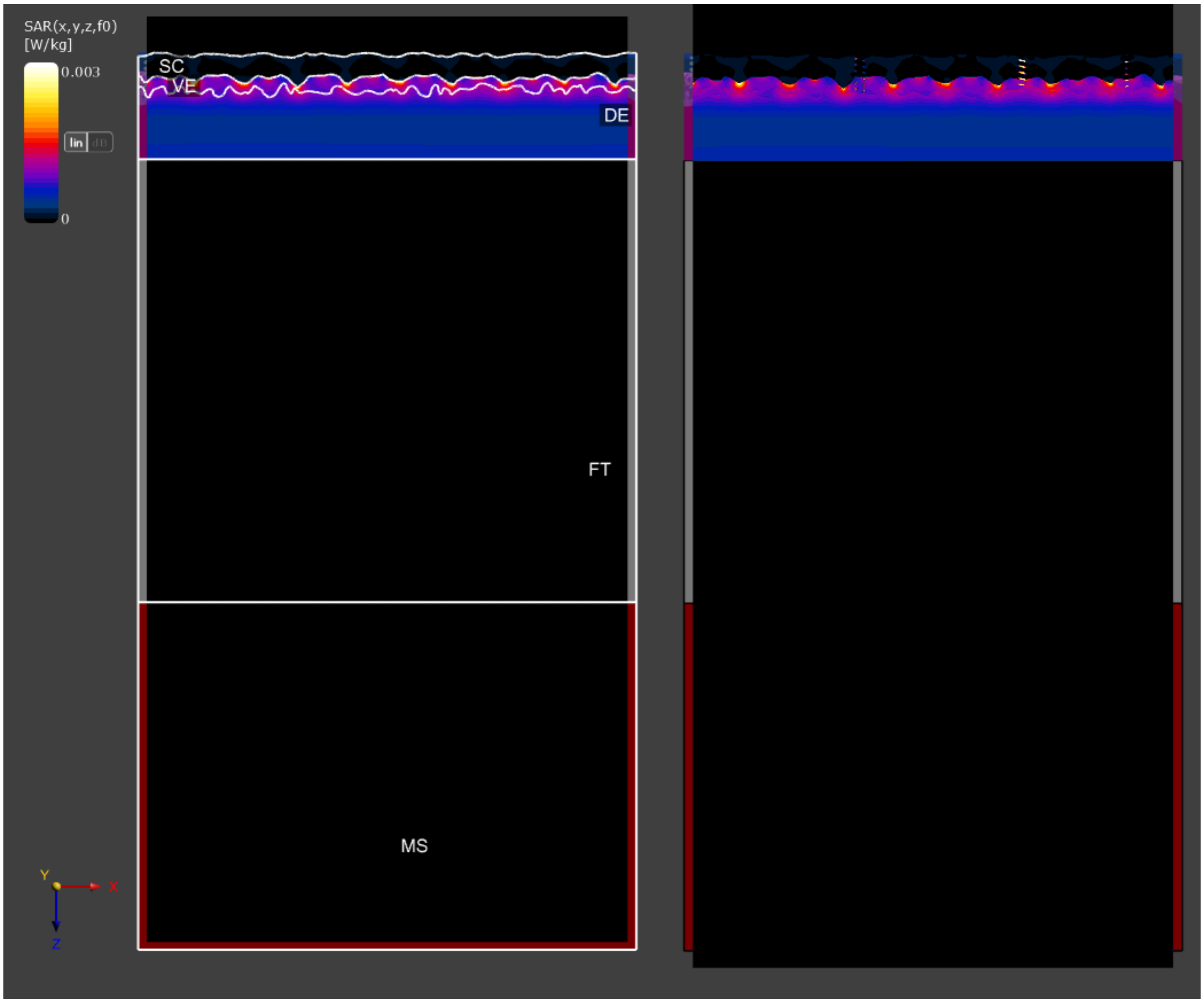

Figure 11. Colormaps of SAR values inside realistic 3D skin models at a plane parallel to the xz-plane for hypothenar region (center), and (c) fingertip (bottom). Values correspond to an incident plane wave of 1V/m in amplitude and 27.5 GHz in frequency, propagating along z axis. The E-field is linearly polarized parallel to x axis.

Table 4. The comparison of mass-averaged SAR values between sweat gland ducts and their surrounding tissue

Skin Layer / Appendage	Mass-Averaged SAR (mW/kg)
Stratum Corneum (SC)	0.089
Viable Epidermis (VE)	0.992
Sweat gland ducts (acrosyringia) outer part	0.061
Sweat gland ducts (acrosyringia) inner part (sweat)	1.857

For the Basal Cell Carcinoma (BCC) case study, marginal differences in both E-field and induced SAR values are identified (Figures 12-13). An increase in the reflected E-field in agreement with the literature [50] and a decrease in SAR values of the layers superficial to BCC region at 27.5GHz is also observed.

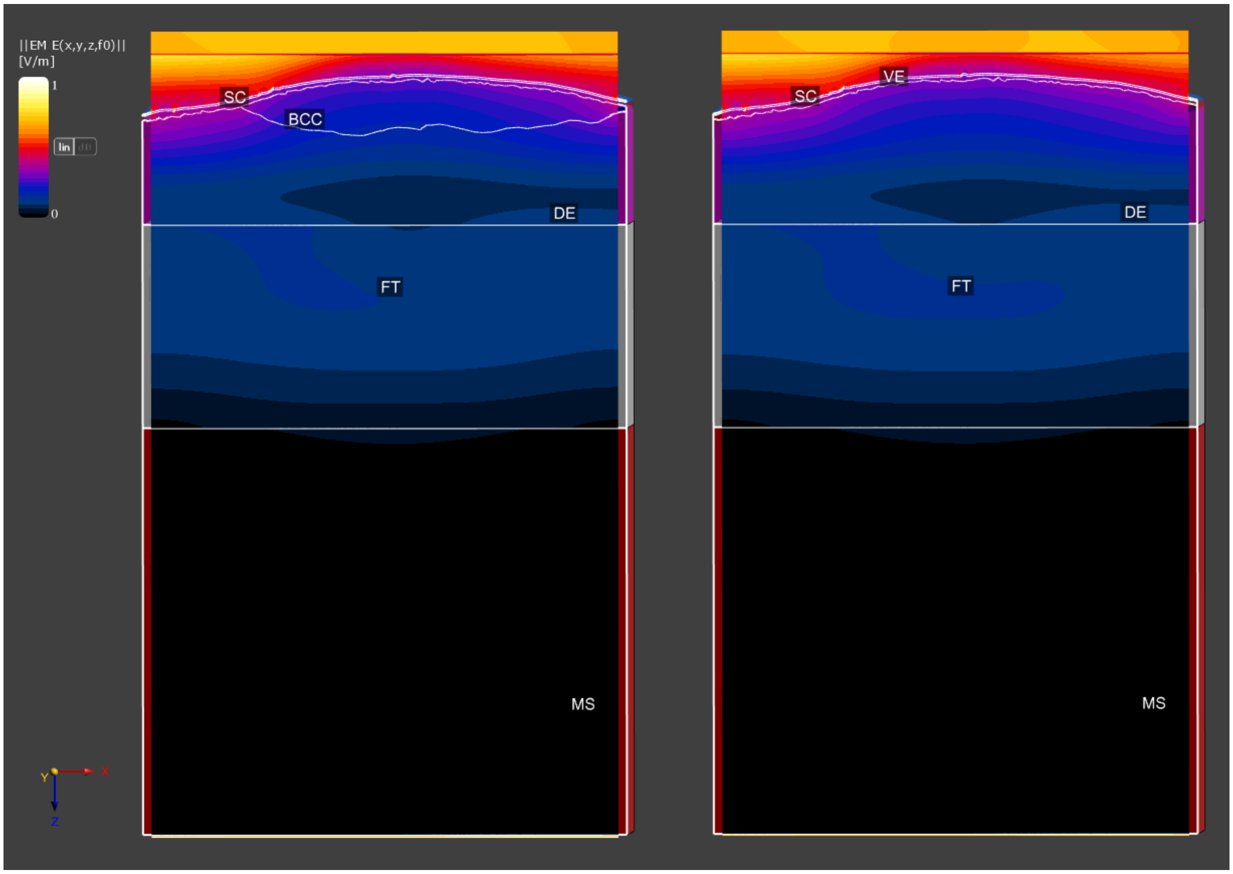

Figure 12. Colormaps of E-field values inside realistic 3D skin models at a plane parallel to the xz-plane for nodular BCC (left), and with no tumor included (right). Values correspond to an incident plane wave of 1V/m in amplitude and 27.5 GHz in frequency, propagating along z axis. The E-field is linearly polarized parallel to x axis.

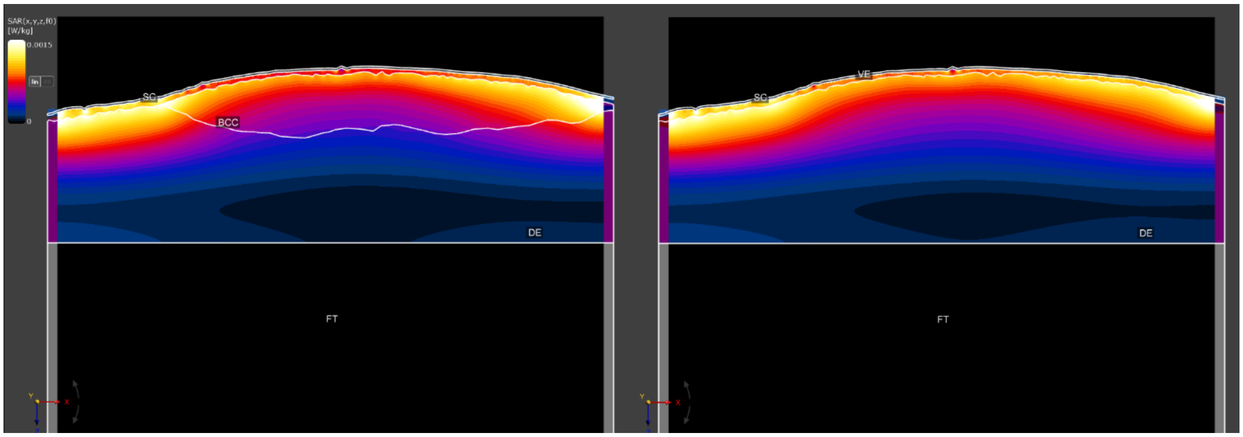

Figure 13. Colormaps of SAR values inside realistic 3D skin models at a plane parallel to the xz-plane for nodular BCC (left), and with no tumor included (right). Values correspond to an incident plane wave of 1V/m in amplitude and 27.5 GHz in frequency, propagating along z axis. The E-field is linearly polarized parallel to x axis.

5 Conclusions

This deliverable presents a comprehensive framework for constructing realistic 3D human skin models and using them for detailed electromagnetic dosimetric analysis at MMW frequencies, with a focus on 27.5 GHz. By integrating high-resolution-OCT and US imaging data, we developed anatomically accurate skin models that reproduce the intra-individual variability across different body sites. These models capture microstructural features, including sweat gland ducts and pathological conditions such as Basal Cell Carcinoma (BCC), which are shown to affect local electromagnetic field distributions and SAR values.

Our findings clearly demonstrate that simplified planar models fail to capture the complexity and variability of E-field and SAR distributions observed in realistic skin geometries. The undulating nature of skin layers, the varying thickness of strata, and the inclusion of microstructures all contribute to substantial deviations in dosimetric outcomes. Furthermore, the selection of appropriate grid resolution in FDTD simulations is shown to be critical for achieving accurate results, especially when dealing with fine anatomical detail.

Overall, the methodology presented in this deliverable identifies the skin microscopic structures that maximize dosimetry (i.e., undulation of layer interfaces), enhances the precision of localized dosimetric assessments, and supports the broader goals of the SEAWave project, including individualized exposure assessment and the development of reliable, simplified phantoms for compliance testing.

6 References

[1] M. C. Ziskin, S. I. Alekseev, K. R. Foster, and Q. Balzano, “Tissue models for RF exposure evaluation at frequencies above 6 GHz,” Apr. 01, 2018, Wiley-Liss Inc. doi: 10.1002/bem.22110.

[2] T. Wu, T. S. Rappaport, and C. M. Collins, “Safe for generations to come: Considerations of safety for millimeter waves in wireless communications,” IEEE Microw Mag, vol. 16, no. 2, pp. 65–84, Mar. 2015, doi: 10.1109/MMM.2014.2377587.

[3] S. I. Alekseev and M. C. Ziskin, “Human skin permittivity determined by millimeter wave reflection measurements,” Bioelectromagnetics, vol. 28, no. 5, pp. 331–339, Jul. 2007, doi: 10.1002/bem.20308.

[4] A. Christ, T. Samaras, E. Neufeld, and N. Kuster, “Transmission coefficient of power density into skin tissue between 6 and 300 ghz,” Radiat Prot Dosimetry, vol. 192, no. 1, pp. 113–118, Oct. 2020, doi: 10.1093/rpd/ncaa179.

[5] Z. Haider, Y. Le Drean, G. Sacco, D. Nikolayev, R. Sauleau, and M. Zhadobov, “High-Resolution Model of Human Skin Appendages for Electromagnetic Dosimetry at Millimeter Waves,” IEEE Journal of Microwaves, vol. 2, no. 1, pp. 214–227, Nov. 2021, doi: 10.1109/jmw.2021.3126712.

[6] Z. Vilagosh, N. Foroughimehr, A. Lajevardipour, and A. W. Wood, “FDTD Simulations of Sweat Ducts and Hair at 0.45 THz,” Dermato, vol. 3, no. 1, pp. 69–84, Mar. 2023, doi: 10.3390/dermato3010006.

[7] A. R. Eldamak, S. Thorson, and E. C. Fear, “Study of the dielectric properties of artificial sweat mixtures at microwave frequencies,” Biosensors (Basel), vol. 10, no. 6, Jun. 2020, doi: 10.3390/BIOS10060062.

[8] Y. Feldman, A. Puzenko, P. Ben Ishai, A. Caduff, and A. J. Agranat, “Human skin as arrays of helical antennas in the millimeter and submillimeter wave range,” in 2008 33rd International Conference on Infrared, Millimeter and Terahertz Waves, 2008, pp. 1–2. doi: 10.1109/ICIMW.2008.4665663.

[9] G. Sacco, S. Pisa, and M. Zhadobov, “Age-dependence of electromagnetic power and heat deposition in near-surface tissues in emerging 5G bands,” Sci Rep, vol. 11, no. 1, Dec. 2021, doi: 10.1038/s41598-021-82458-z.

[10] A. Christ, T. Samaras, E. Neufeld, and N. Kuster, “Rf-induced temperature increase in a stratified model of the skin for plane-wave exposure at 6-100 ghz,” Radiat Prot Dosimetry, vol. 188, no. 3, pp. 350–360, Jun. 2020, doi: 10.1093/rpd/ncz293.

[11] A. Christ, A. Aeschbacher, F. Rouholahnejad, T. Samaras, B. Tarigan, and N. Kuster, “Reflection Properties of the Human Skin From 40 to 110 GHz: A Confirmation Study,” Bioelectromagnetics, vol. 42, no. 7, pp. 562–574, Oct. 2021, doi: 10.1002/bem.22362.

[12] G. Shafirstein and E. G. Moros, “Modelling millimetre wave propagation and absorption in a high resolution skin model: The effect of sweat glands,” Phys Med Biol, vol. 56, no. 5, pp. 1329–1339, Mar. 2011, doi: 10.1088/0031-9155/56/5/007.

[13] K. Sasaki, M. Mizuno, K. Wake, and S. Watanabe, “Monte Carlo simulations of skin exposure to electromagnetic field from 10 GHz to 1 THz,” Phys Med Biol, vol. 62, no. 17, pp. 6993–7010, Aug. 2017, doi: 10.1088/1361-6560/aa81fc.

[14] F. Schönborn, K. Poković, and N. Kuster, “Dosimetric Analysis of the Carousel Setup for the Exposure of Rats at 1.62 GHz,” Bioelectromagnetics, vol. 25, no. 1, pp. 16–26, Jan. 2004, doi: 10.1002/bem.10153.

[15] L. B. Sasser, J. E. Morris, B. W. Wilson, and L. E. Anderson, “Genotoxic Potential of 1.6 GHz Wireless Communication Signal: In Vivo Two-Year Bioassay,” Radiat Res, vol. 159, no. 4, pp. 558–564, Apr. 2003, doi: 10.1667/0033-7587(2003)159[0558:GPOGWC]2.0.CO;2.

[16] A. Peyman, A. A. Rezazadeh, and C. Gabriel, “Changes in the dielectric properties of rat tissue as a function of age at microwave frequencies,” 2001. [Online]. Available: www.iop.org/Journals/pbPII:S0031-9155

[17] T. Wu, A. Hadjem, M. F. Wong, A. Gati, O. Picon, and J. Wiart, “Whole-body new-born and young rats’ exposure assessment in a reverberating chamber operating at 2.4 GHz,” Phys Med Biol, vol. 55, no. 6, pp. 1619–1630, 2010, doi: 10.1088/0031-9155/55/6/006.

[18] R. Pinto et al., “Dosimetry of a set-up for the exposure of newborn mice to 2.45-GHz WIFI frequencies,” Radiat Prot Dosimetry, vol. 140, no. 4, pp. 326–332, Apr. 2010, doi: 10.1093/rpd/ncq129.

[19] L. Ardoino, V. Lopresto, S. Mancini, C. Marino, R. Pinto, and G. A. Lovisolo, “A radio-frequency system for in vivo pilot experiments aimed at the studies on biological effects of electromagnetic fields,” Phys Med Biol, vol. 50, no. 15, pp. 3643–3654, Aug. 2005, doi: 10.1088/0031-9155/50/15/011.

[20] A. Khadir Fall, C. Lemoine, P. Besnier, R. Sauleau, Y. Le Dréan, and M. Zhadobov, “Exposure Assessment in Millimeter-Wave Reverberation Chamber Using Murine Phantoms,” Bioelectromagnetics, vol. 41, no. 2, pp. 121–135, Feb. 2020, doi: 10.1002/bem.22243.

[21] S. I. Alekseev, O. V. Gordiienko, and M. C. Ziskin, “Reflection and penetration depth of millimeter waves in murine skin,” Bioelectromagnetics, vol. 29, no. 5, pp. 340–344, Jul. 2008, doi: 10.1002/bem.20401.

[22] Y. Gong et al., “Life-Time Dosimetric Assessment for Mice and Rats Exposed in Reverberation Chambers for the Two-Year NTP Cancer Bioassay Study on Cell Phone Radiation,” IEEE Trans Electromagn Compat, vol. 59, no. 6, pp. 1798–1808, Dec. 2017, doi: 10.1109/TEMC.2017.2665039.

[23] V. De Santis, A. Di Fracesco, K. R. Foster, G. Bit-Babik, and A. Faraone, “Monte-Carlo based Numerical Dosimetry in Reverberation Chamber Exposure Systems Employed for In-Vivo Rodent Bioassays,” IEEE Access, 2023, doi: 10.1109/ACCESS.2023.3251889.

[24] S. Iakovidis, S. Leonardi, E. Fratini, S. Pazzaglia, M. Mancuso, and T. Samaras, “Murine Skin Dosimetry Under Millimeter Wave Exposure,” IEEE Journal of Microwaves, vol. 4, no. 2, pp. 204–212, Apr. 2024, doi: 10.1109/JMW.2023.3345133.

[25] “SEAWave project.” Accessed: Sep. 28, 2023. [Online]. Available: https://seawave-project.eu/

[26] C. Marino et al., “Gaps in Knowledge Relevant to the ‘iCNIRP Guidelines for Limiting Exposure to Time-Varying Electric, Magnetic and Electromagnetic Fields (100 kHz to 300 GHz),’” Health Phys, 2024, doi: 10.1097/HP.0000000000001944.

[27] H. Wang et al., “Millimeter waves in medical applications: status and prospects,” Feb. 01, 2024, Chinese Medical Association. doi: 10.1016/j.imed.2023.07.002.

[28] J. Welzel, “Optical coherence tomography in dermatology: A review,” 2001. doi: 10.1034/j.1600-0846.2001.007001001.x.

[29] F. Latriglia et al., “Line-Field Confocal Optical Coherence Tomography (LC-OCT) for Skin Imaging in Dermatology,” Life, vol. 13, no. 12, Dec. 2023, doi: 10.3390/life13122268.

[30] S. Adabi et al., “Universal in vivo Textural Model for Human Skin based on Optical Coherence Tomograms,” Sci Rep, vol. 7, no. 1, Dec. 2017, doi: 10.1038/s41598-017-17398-8.

[31] “Atlas of Ultrasound-Guided Procedures in Interventional Pain Management.”

[32] P. J. Caspers, G. W. Lucassen, E. A. Carter, H. A. Bruining, and G. J. Puppels, “In Vivo Confocal Raman Microspectroscopy of the Skin: Noninvasive Determination of Molecular Concentration Pro®les.”

[33] K. Sasaki, K. Wake, and S. Watanabe, “Measurement of the dielectric properties of the epidermis and dermis at frequencies from 0.5GHz to 110GHz,” Phys Med Biol, vol. 59, no. 16, pp. 4739–4747, Aug. 2014, doi: 10.1088/0031-9155/59/16/4739.

[34] N. Nakagawa, M. Matsumoto, and S. Sakai, “In vivo measurement of the water content in the dermis by confocal Raman spectroscopy,” Skin Research and Technology, vol. 16, no. 2, pp. 137–141, May 2010, doi: 10.1111/j.1600-0846.2009.00410.x.

[35] N. Betzalel, P. Ben Ishai, S. Einav, and Y. Feldman, “The AC conductivity of human sweat ducts as the dominant factor in the sub-THz reflection coefficient of skin,” J Biophotonics, vol. 14, no. 7, Jul. 2021, doi: 10.1002/jbio.202100027.

[36] P. A. Hasgall et al., “ IT’IS Database for Thermal and Electromagnetic Parameters of Biological Tissues, Version 4.1.”

[37] H. Fruhstorfer, U. Abel, C. D. Garthe, and A. Knüttel, “Thickness of the stratum corneum of the volar fingertips,” Clinical Anatomy, vol. 13, no. 6, pp. 429–433, 2000, doi: 10.1002/1098-2353(2000)13:6<429::AID-CA6>3.0.CO;2-5.

[38] M. Egawa, T. Hirao, and M. Takahashi, “In vivo estimation of stratum corneum thickness from water concentration profiles obtained with raman spectroscopy,” Acta Derm Venereol, vol. 87, no. 1, pp. 4–8, 2007, doi: 10.2340/00015555-0183.

[39] D. A. Lintzeri, N. Karimian, U. Blume-Peytavi, and J. Kottner, “Epidermal thickness in healthy humans: a systematic review and meta-analysis,” Aug. 01, 2022, John Wiley and Sons Inc. doi: 10.1111/jdv.18123.

[40] S. Usami, M. Okazaki, T. Nitta, N. Uemura, T. Homma, and K. Akita, “Histological investigation of common insensate flaps obtained from the hand and forearm regions for use in fingertip reconstruction,” J Plast Surg Hand Surg, vol. 51, no. 3, pp. 182–186, May 2017, doi: 10.1080/2000656X.2016.1213733.

[41] D. Crisan, M. Lupsor, A. Boca, M. Crisan, and R. Badea, “Ultrasonographic assessment of skin structure according to age,” Indian J Dermatol Venereol Leprol, vol. 78, no. 4, p. 519, Jul. 2012, doi: 10.4103/0378-6323.98096.

[42] E.S. Gadelmawla, M.M. Koura, T.M.A. Maksoud, I.M. Elewa, H.H. Soliman, “Roughness parameters”, Journal of Materials Processing Technology, vol. 123, Issue 1, 2002, p. 133-145, https://doi.org/10.1016/S0924-0136(02)00060-2.

[43] A. Mirbeik-Sabzevari, R. Ashinoff and N. Tavassolian, "Ultra-Wideband Millimeter-Wave Dielectric Characteristics of Freshly Excised Normal and Malignant Human Skin Tissues," in *IEEE Transactions on Biomedical Engineering*, vol. 65, no. 6, pp. 1320-1329, June 2018, doi: 10.1109/TBME.2017.2749371

[44] I. Laakso, “Assessment of the computational uncertainty of temperature rise and SAR in the eyes and brain under far-field exposure from 1 to 10 GHz,” Phys Med Biol, vol. 54, no. 11, pp. 3393–3404, 2009, doi: 10.1088/0031-9155/54/11/008.

[45] A. Taflove and S. C. Hagness, Computational Electrodynamics: The Finite-Difference Time-Domain Method, Third Edition, Third. Artech House.

[46] A. J. Kogon and C. D. Sarris, “Finite-Difference Time-Domain Modeling of Periodic Structures: A review of constant wave vector techniques,” Jun. 01, 2022, IEEE Computer Society. doi: 10.1109/MAP.2021.3061023.

[47] A. L. Kapetanović, G. Sacco, D. Poljak, and M. Zhadobov, “Area-Averaged Transmitted and Absorbed Power Density on a Realistic Ear Model,” IEEE J Electromagn RF Microw Med Biol, vol. 7, no. 1, pp. 39–45, Mar. 2023, doi: 10.1109/JERM.2022.3225380.

[48] M. Colella, S. Di Meo, M. Liberti, M. Pasian, and F. Apollonio, “Advantages and Disadvantages of Computational Dosimetry Strategies in the Low mmW Range: Comparison between Multilayer Slab and Anthropomorphic Models,” IEEE Trans Microw Theory Tech, vol. 71, no. 10, pp. 4533–4545, Oct. 2023, doi: 10.1109/TMTT.2023.3267568.

[49] X. Xu, C. Yu, L. Xu, and J. Xu, “Emerging roles of keratinocytes in nociceptive transduction and regulation,” Sep. 09, 2022, Frontiers Media S.A. doi: 10.3389/fnmol.2022.982202.

[50] A. Mirbeik-Sabzevari and N. Tavassolian, “Tumor Detection Using Millimeter-Wave Technology: Differentiating Between Benign Lesions and Cancer Tissues,” IEEE Microwave Magazine, vol. 20, no. 8, pp. 30-43, Aug. 2019, doi: 10.1109/MMM.2019.2915472.